# Excess pore water pressure behavior of saturated soft clay under cyclic confining pressure with different frequencies

Juehao Huang[1,2], Jun Hu[3]*, Hongchao Wang[4], Jian Chen[1,2] and Shuai Liu[3]

[1]State Key Laboratory of Geomechanics and Geotechnical Engineering, Institute of Rock and Soil Mechanics, Chinese Academy of Sciences, Wuhan, China, [2]School of Engineering Science, University of Chinese Academy of Sciences, Beijing, China, [3]School of Civil Engineering, Chang'an University, Xi'an, China, [4]China Railway Eryuan Engineering Group Co Ltd., Chengdu, China

The excess pore water pressure is main factor affecting the dynamic response of saturated soft clay under traffic loads. Recognize that, cyclic triaxial tests with and without cyclic confining pressure were carried out to study the development of excess pore water pressure of saturated soft clay. The impacts of factors, such as cyclic stress ratio (CSR), loading frequency, and cyclic confining pressure, were analyzed. Excess pore water pressure increases with increasing cyclic stress ratios, while decreases with increasing loading frequencies. Nevertheless, with increasing cyclic confining pressures, the maximum excess pore water pressure increases, while the minimum excess pore water pressure remains unchanged. Besides that, the greater CSR and cyclic confining pressure deliver an increment of both maximum and minimum excess pore water pressure rate. However, the excess pore water pressure rate - time curves coincide under different loading frequencies. Meanwhile, both the normalized maximum and minimum excess pore water pressure rates are linearly proportional with time under different test conditions in logarithmic coordinates. Based on that, both maximum and minimum excess pore water pressure prediction models, relating to the above factors, are proposed, and the predicted results accord well with the measured data.

KEYWORDS

saturated soft clay, cyclic triaxial test, cyclic confining pressure, frequency, excess pore water pressure

## 1 Introduction

Many traffic infrastructures have been constructed, especially on soft clay subgrade (Huang et al., 2020; Huang et al., 2020a; Huang et al., 2020b). The traffic loading induced excess pore water pressure not only leads to additional deformation but also results in the degradation of soil strength (Wichtmann et al., 2013; Jiang et al., 2018). Therefore, it is necessary to study the development of excess pore water pressure of soft clay to properly design and plan transportation facilities on soft clay subsoils.

TABLE 1 Physico-mechanical indices of the remolded Ningbo clay.

| Unit weight, γ/ (kN/m3) | Natural water content, w/% | Liquid limit, WL/% | Plasticity limit, Wp/% | Plasticity index, Ip | Coefficient of permeability, k/ (10−8 cm/s) | Void ratio, e | Coefficient of compressibility, av/ MPa−1 | Shear strength parameters | | Particle distribution/% | |
|---|---|---|---|---|---|---|---|---|---|---|---|
| | | | | | | | | Cohesion, ccu (kPa) | Friction angle, φcu (°) | 0.075−0.005/ mm | < 0.005/ mm |
| 17.6 | 43.9 | 51.5 | 23.3 | 28.2 | 5.18 | 1.25 | 0.81 | 11.40 | 15.89 | 41.0 | 59.0 |
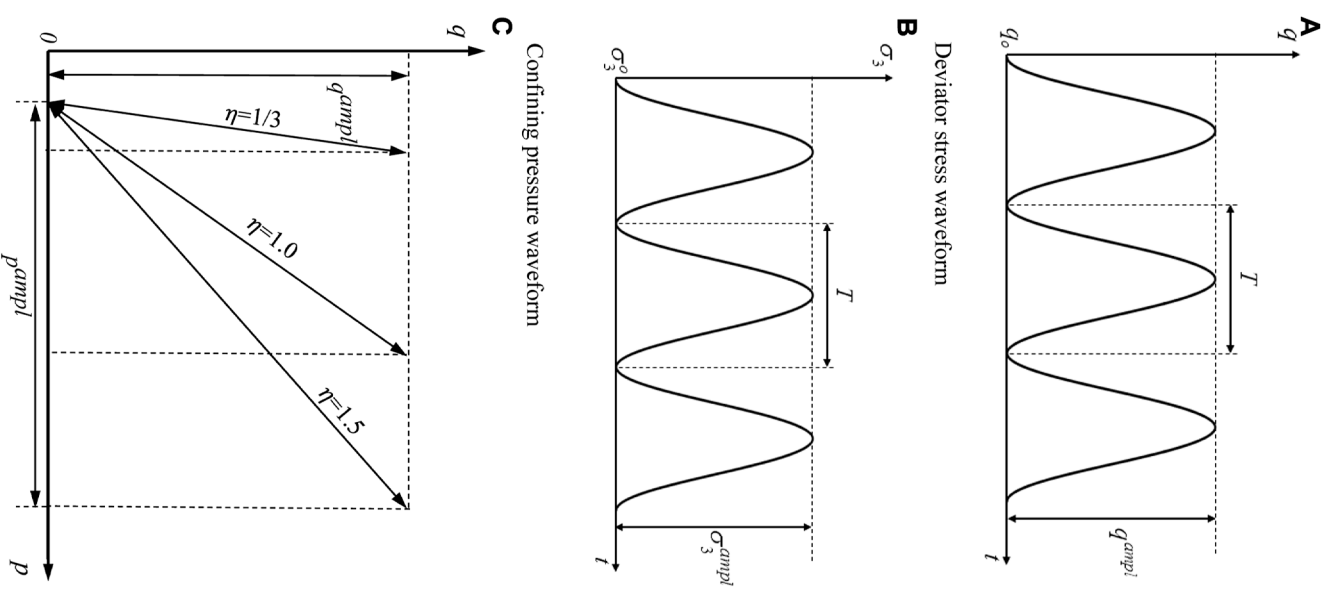


FIGURE 1
(A) Deviator stress waveform; (B) Confining pressure waveform; (C) Diagram of stress path employed in CCP and VCP tests.

Some researchers have conducted experimental investigations on the development of excess pore water pressure (Hyde and Ward 1985; Hyodo et al., 1992; Hyde

TABLE 2 Summary of cyclic triaxial tests.

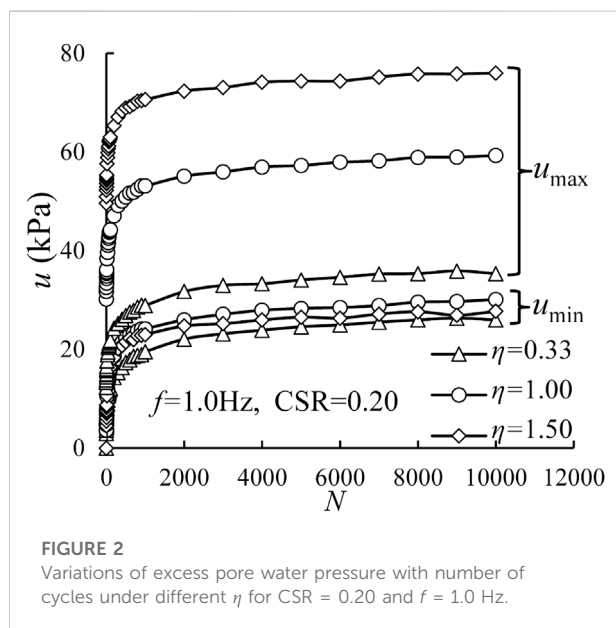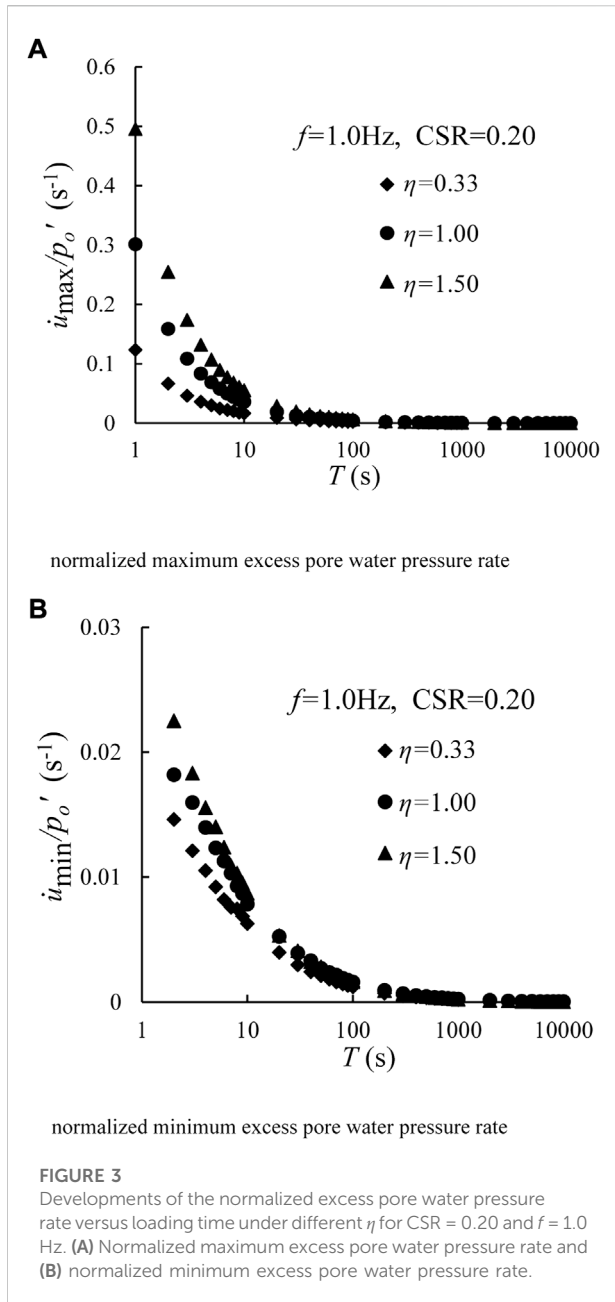| Test no. | $q^{ampl}$/kPa | CSR | $\sigma_3^{ampl}$/kPa | $\eta$ | $f$/Hz | Number of cycles | Drainage conditions |
|---|---|---|---|---|---|---|---|
| P1 | 20 | 0.10 | 0 | 1/3 | 1.0 | 10,000 | Undrained condition |
| | | | 13 | 1.0 | | | |
| | | | 23 | 1.5 | | | |
| P2 | 30 | 0.15 | 0 | 1/3 | 1.0 | | |
| | | | 20 | 1.0 | | | |
| | | | 35 | 1.5 | | | |
| P3 | | | 0 | 1/3 | 0.5 | | |
| | | | 27 | 1.0 | | | |
| | | | 47 | 1.5 | | | |
| P4 | 40 | 0.20 | 0 | 1/3 | 1.0 | | |
| | | | 27 | 1.0 | | | |
| | | | 47 | 1.5 | | | |
| P5 | | | 0 | 1/3 | 2.0 | | |
| | | | 27 | 1.0 | | | |
| | | | 47 | 1.5 | | | |
| P6 | 60 | 0.30 | 0 | 1/3 | 1.0 | | |
| | | | 40 | 1.0 | | | |
| | | | 70 | 1.5 | | | |
| P7 | 50 | 0.25 | 0 | 1/3 | 1.0 | | |
| | | | 33 | 1.0 | | | |
| | | | 58 | 1.5 | | | |



FIGURE 2
Variations of excess pore water pressure with number of cycles under different $\eta$ for CSR = 0.20 and $f$ = 1.0 Hz.

et al., 1993; Wang et al., 2013; Ren et al., 2018; Du et al., 2022; Fu et al., 2022), and many empirical formulas to predict excess pore water pressure have been proposed (Nie et al., 2007; Paul et al., 2014; Cary and Zapata, 2016). For example, Ohara and Matsuda (1988) proposed a hyperbolic model to predict the excess pore water pressure, relating to the number of cycles. Reviewing the previous researches, cyclic triaxial tests with constant confining pressure (CCP tests) have been usually employed, in which only cyclic deviator stress was used to simulate the traffic loading. However, it has been widely recognized that the CCP tests are not appropriate for reflecting the real conditions induced by the traffic.

The real traffic-induced stress field acting on the soil elements is composed of a simultaneous cyclic variation of deviator stress, confining pressure, and shear stress (Lekarp et al., 2000). The traffic loading is often simulated with the simultaneous application of the cyclic confining pressure and cyclic deviator stress in laboratory tests, i.e., cyclic triaxial tests with variable confining pressure (VCP tests) (Wichtmann et al., 2007; Rondon et al., 2009; Cai et al., 2013; Gu et al., 2016, 2017). For example, Rondon et al. (2009) found that the deformation of unbound granular materials (UGMs) under CCP tests was underestimated, compared with that under VCP tests. Additionally, both the development of excess pore water pressures and accumulated axial strains of soft clay were influenced significantly by cyclic confining pressure (Cai et al., 2013). Gu et al. (2016) found that the development of permanent volumetric strain and axial strain speeded up with increasing cyclic confining pressure for overconsolidated and normally-

**FIGURE 3**
Developments of the normalized excess pore water pressure rate versus loading time under different $\eta$ for CSR = 0.20 and $f$ = 1.0 Hz. **(A)** Normalized maximum excess pore water pressure rate and **(B)** normalized minimum excess pore water pressure rate.



**FIGURE 4**
Variations of excess pore water pressure with number of cycles under different CSRs for $f$ = 1.0 Hz and $\eta$ = 1.00.

consolidated specimens. All these studies indicated that the effect of cyclic confining pressure cannot be ignored.

Besides, the response frequency of soft clay under train loads changes continuously with the train passing (Tang et al., 2008; Gu et al., 2012; Guo et al., 2013; Yang et al., 2018; Zhou et al., 2022). Some experimental investigations, such as those by Matsui et al. (1992), and Guo et al. (2016), have studied the effect of loading frequency on mechanical behaviors of soils under cyclic loading. However, there are conflicting observations regarding this problem. For example, Hyde et al. (1993) conducted CCP tests on Ariake clay and found that the development of excess pore water pressure was independent of frequency. Guo et al.
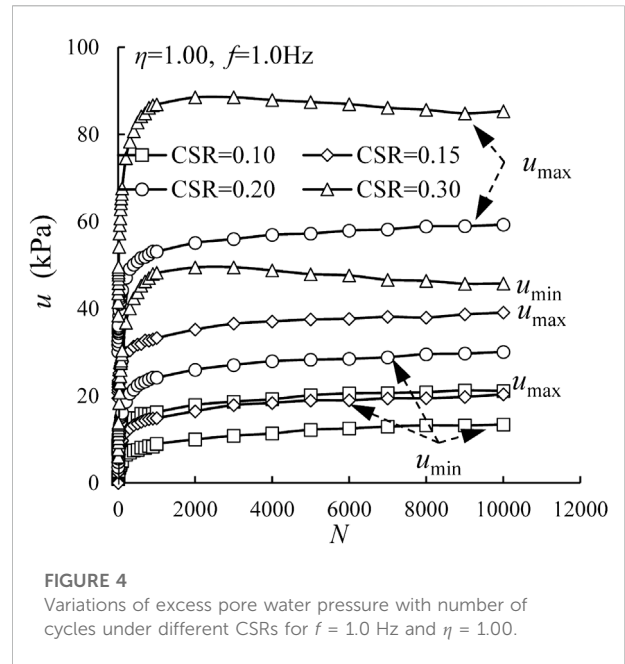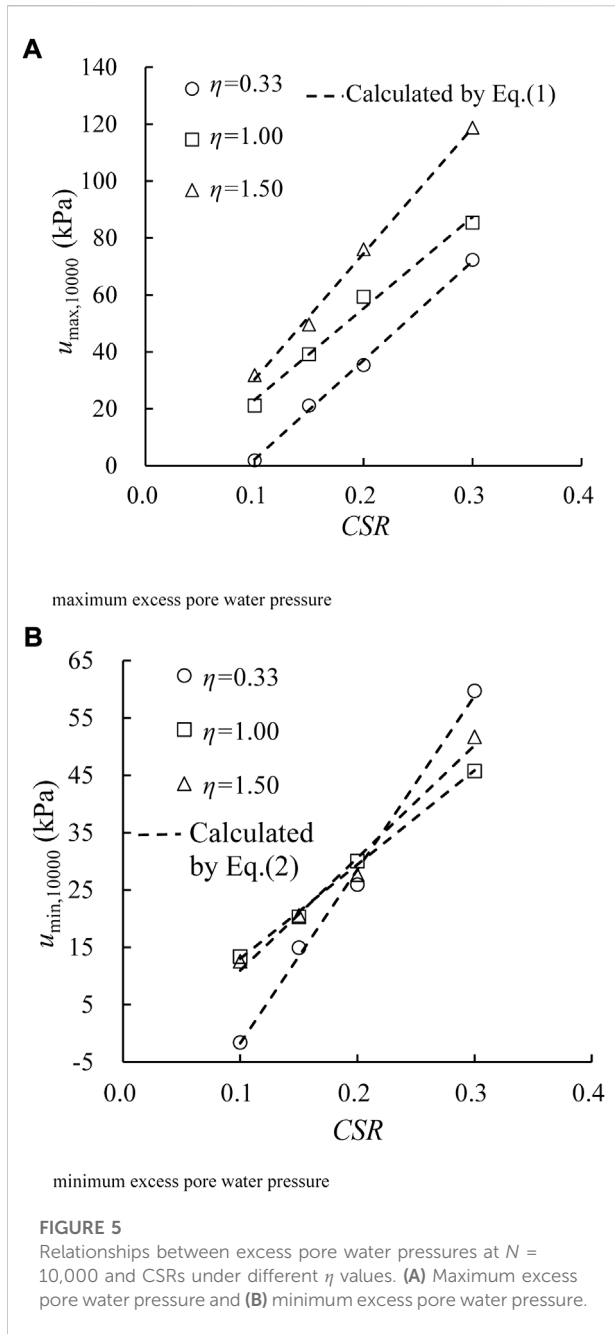
(2016) found that the lower frequency delivered the larger vertical strain. However, the effect of cyclic confining pressure was not taken into consideration in their study. Therefore, the impacts of loading frequency and cyclic confining pressure on the mechanical behaviors of soils under traffic loads need to study in-depth.

This study consists of three parts: firstly, both CCP and VCP tests were carried out under undrained conditions, and the development of excess pore water pressure was evaluated and compared under different cyclic confining pressures, CSRs, and loading frequencies; Then, maximum and minimum excess pore water pressure prediction models were proposed and the effects of cyclic confining pressures, CSRs, and loading frequencies on fitting parameters were analyzed in detail. Finally, the verifications of models were made based on other test data.

## 2 Experimental program

### 2.1 Test materials

The original clays were sampled about a depth of 28.0–30.0 m beneath the ground surface from Jiangshan Station of Ningbo subway line No. 3 in Ningbo city, China. To eliminate the effect of soil structure and obtain specimens with good homogeneity, the remolded samples were used in this study. Table 1 shows the physico-mechanical indices of the tested clay following MWR (2019, GB/T 50123-2019), indicating that the tested soil was classified as CH (i.e., high plasticity) according to the Unified Soil Classification System (USCS) soil classification method of ASTM (2017).
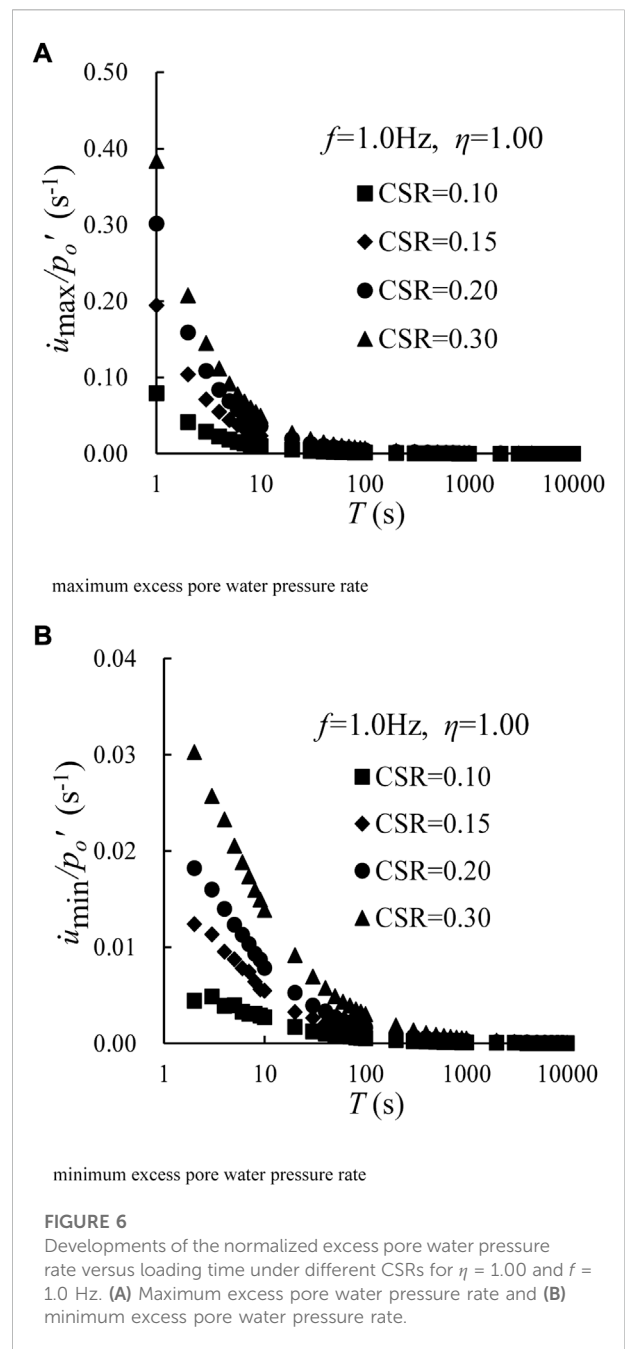
maximum excess pore water pressure

minimum excess pore water pressure

**FIGURE 5**
Relationships between excess pore water pressures at $N =$ 10,000 and CSRs under different $\eta$ values. **(A)** Maximum excess pore water pressure and **(B)** minimum excess pore water pressure.

TABLE 3 Fitting parameters under different conditions.

| $\eta$ | $u_{\max,10000} = e + f \cdot CSR$ | | | $u_{\min,10000} = m + n \cdot CSR$ | | |
|---|---|---|---|---|---|---|
| | $e$ | $f$ | $R^2$ | $m$ | $n$ | $R^2$ |
| 1/3 | −32.673 | 348.23 | 0.998 | −31.958 | 302.61 | 0.995 |
| 1.0 | −9.020 | 321.16 | 0.989 | −3.368 | 164.05 | 0.997 |
| 1.5 | −13.880 | 441.93 | 0.997 | −8.618 | 196.07 | 0.984 |



maximum excess pore water pressure rate

minimum excess pore water pressure rate

**FIGURE 6**
Developments of the normalized excess pore water pressure rate versus loading time under different CSRs for $\eta = 1.00$ and $f = 1.0$ Hz. **(A)** Maximum excess pore water pressure rate and **(B)** minimum excess pore water pressure rate.

## 2.2 Test procedures

The advanced cyclic triaxle device (i.e., DYNTTS) was employed. The axial deviator stress and confining pressure can vary simultaneously with multiple loading waveforms, such as triangular, sinusoidal, square, and customized wave shapes.

According to MWR (2019, GB/T 50123-2019, 2019), cylindrical specimens (i.e., diameter: 38 mm and height: 76 mm) were prepared and mounted in the triaxle cell. Following this, all of the remolded specimens were
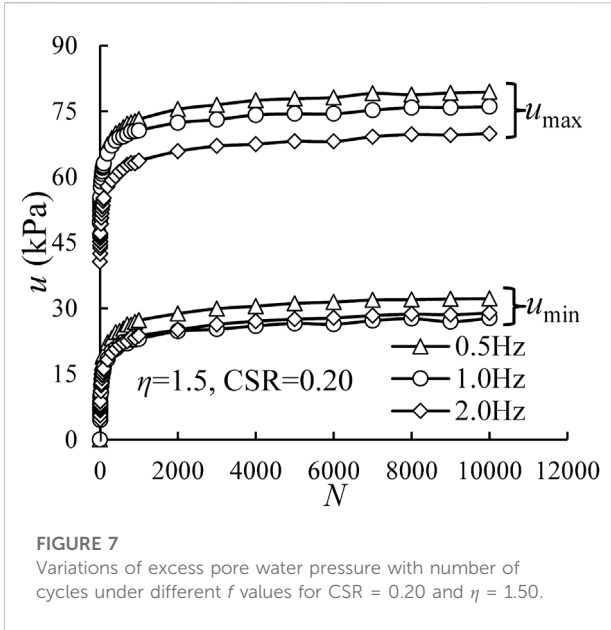
FIGURE 7
Variations of excess pore water pressure with number of cycles under different $f$ values for CSR = 0.20 and $\eta$ = 1.50.



maximum excess pore water pressure rate



minimum excess pore water pressure rate

FIGURE 8
Developments of the normalized excess pore water pressure rate versus loading time under different $f$ values for $\eta$ = 1.50 and CSR = 0.20. **(A)** Maximum excess pore water pressure rate and **(B)** minimum excess pore water pressure rate.

saturated at a back pressure of 300 kPa with an effective stress of 20 kPa, until all samples were saturated completely (namely, Skempton's B value more than 0.95). After that, the specimens were isotropically consolidated. When the drainage volume was less than 100 mm³/h, the consolidation was considered completed (Sun et al., 2015). Finally, considering the low permeability of the tested specimens, cyclic loading was applied under undrained conditions.

To simulate traffic loading as reality as possible, cyclic deviator stress and cyclic confining pressures were applied with a phase difference of zero in semi-sine wave (Cai et al., 2013). For the sake of analysis, the cyclic stress ratio (CSR) is employed (Sakai et al., 2003). CSR is defined as CSR = $q^{ampl}/p_o'$, where $q^{ampl}$ is the amplitude of the cyclic deviator stress, and $p_o'$ is initial effective mean principal stress. Moreover, parameter $\eta$ is selected to depict the slope of stress path (Cai et al., 2013; Gu et al., 2016, 2017) as shown in Figure 1, and defined as the ratio of $p^{ampl}$ to $q^{ampl}$, where $p^{ampl}$ is the amplitude of the cyclic mean principle total stress, and defined as $p^{ampl} = (\sigma_1^{ampl} + 2\sigma_3^{ampl})/3$. $\sigma_1^{ampl}$ is the amplitude of the cyclic axial total stress, and $\sigma_3^{ampl}$ is the amplitude of the cyclic confining pressure.

Herein, five CSR values of 0.10, 0.15, 0.20, 0.25, and 0.30 are employed. At a certain CSR, the selection of $\eta$ values depends on the operation situation of the advance advice in the laboratory. The greater $\eta$ value leads to the more badly wear of sealing rings of the confining pressure controller, directly causing the instability of the loading waveform. Therefore, for a specific CSR, $\eta$ = 1/3, 1.0, and 1.5 were employed, in which $\eta$ = 1/3 represented CCP tests and $\eta$ = 1.0 and 1.5 represented VCP tests. Additionally, it should be noted that the maximum
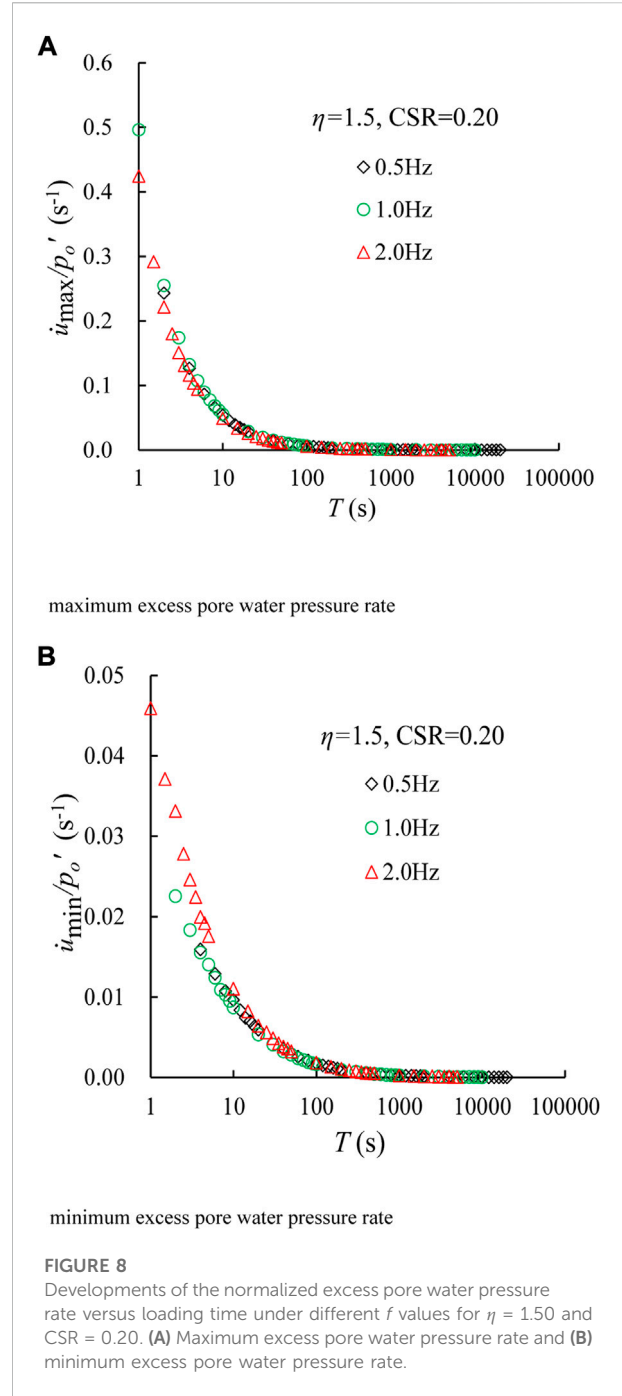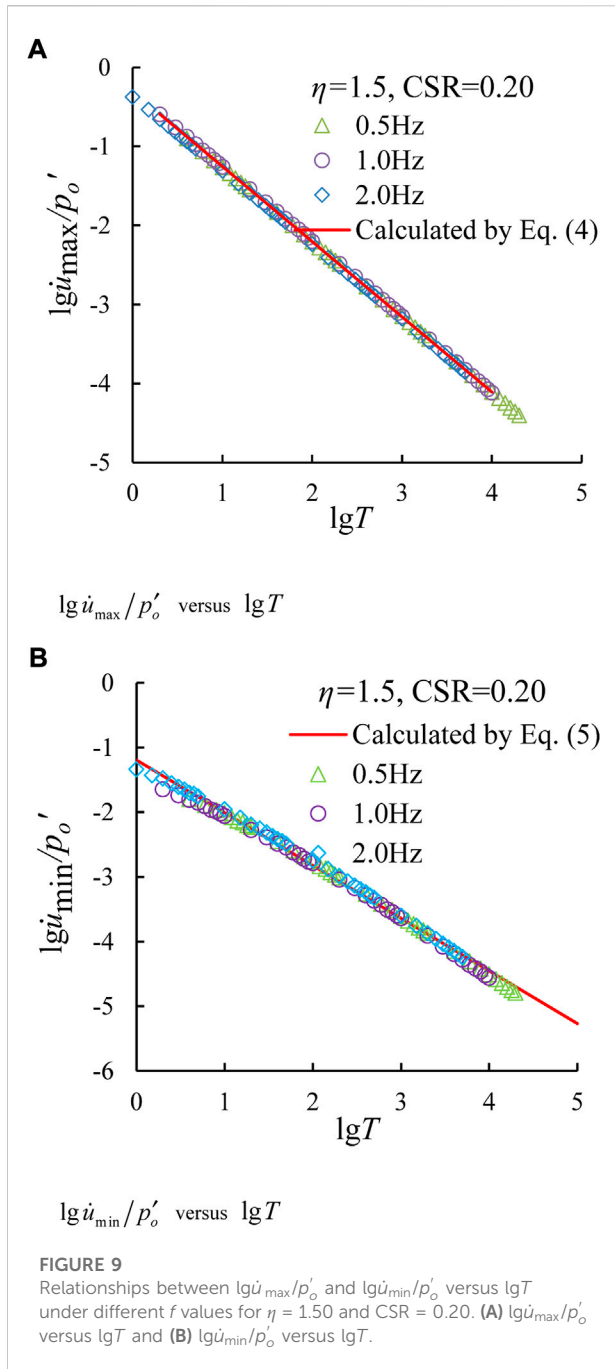
frequency of the device used in the test is 5 Hz, and the frequency of $q^{ampl}$ and $\sigma_3^{ampl}$ cannot be controlled independently. Therefore, the frequency of $q^{ampl}$ and $\sigma_3^{ampl}$ was consistent in tests. Following the researches of Tang et al. (2008), the response frequency of saturated soft clay around the tunnel are high frequency (i.e., 2.5–2.8 Hz) and low frequency (i.e., 0.4–0.6 Hz) around the subway tunnel. Meanwhile, the greater frequency can cause an unstable waveform of cyclic confining pressure. Therefore, combining

$\lg \dot{u}_{\max}/p'_o$ versus $\lg T$

$\lg \dot{u}_{\min}/p'_o$ versus $\lg T$

**FIGURE 9**
Relationships between $\lg \dot{u}_{\max}/p'_o$ and $\lg \dot{u}_{\min}/p'_o$ versus $\lg T$ under different $f$ values for $\eta = 1.50$ and CSR = 0.20. **(A)** $\lg \dot{u}_{\max}/p'_o$ versus $\lg T$ and **(B)** $\lg \dot{u}_{\min}/p'_o$ versus $\lg T$.

with the laboratory results, three frequencies of 0.5, 1.0, and 2.0 Hz were employed. Besides, the greater number of cycles can also wear the rubber sealing ring of the axial loading system, resulting in leakage from the triaxial cell. Therefore, all specimens were subjected to 10,000 cycles (Guo et al., 2013; Wang et al., 2020). Table 2 presents the details of cyclic triaxial tests. Among them, the tests of P1–P6 were performed to investigate the effects of CSR, cyclic confining pressure, and loading frequency. The test results of P7 were employed to validate the applicability of prediction models.

# 3 Test results

The development of excess pore water pressure of soft clay in CCP and VCP tests are investigated in this study. Further discussions on the test results considering the several factors are detailed as follows, respectively.

## 3.1 Influence of cyclic confining pressure

Figure 2 presents excess pore water pressure (i.e., $u$) versus the number of cycles (i.e., $N$) with different $\eta$ values. The CSR value is 0.20 and the frequency is 1.0 Hz. The maximum and minimum values of excess pore water pressure per cycle are denoted as $u_{\max}$ and $u_{\min}$, respectively. As a whole, both $u_{\max}$ and $u_{\min}$ generally accumulate at the beginning and then tend to be stable with a gradually decreasing accumulation rate. Generally, at a certain number of cycles, $u_{\max}$ is relatively larger under VCP tests comparing with that obtained in CCP tests: the greater amplitude of cyclic confining pressure, the greater maximum excess pore water pressure. For example, when $f = 1.0$ Hz and CSR = 0.20, $u_{\max}$ at $N = 10,000$ are 59.26 and 75.98 kPa under $\eta =$ 1.0, and 1.5, respectively, while it is 35.34 kPa under CCP test ($\eta =$ 0.33). However, $u_{\min}$ remains unchanged under CCP and VCP tests. When $f = 1.0$ Hz and CSR = 0.20, $u_{\min}$ are, 29.95, 30.08, and 27.70 kPa at 10,000 cycles under $\eta =$ 0.33, 1.00, and 1.50, respectively.

Recalling Figure 2, the increasing rates of excess pore water pressure are different under different $\eta$ values. Therefore, the effect of cyclic confining pressure on excess pore water pressure is further analyzed from the perspective of excess pore water pressure rate (i.e., $\dot{u}$). Among that, the parameter $\dot{u}$ is defined as $\dot{u} = u/T$, where $T$ represents loading time and is denoted as $T = N/f$. For simplicity, the excess pore water pressure rate is normalized to initial effective mean principal stress, i.e., $\dot{u}/p'_o = u/(T \cdot p'_o) = u \cdot f/(N \cdot p'_o)$. Based on that, the maximum and minimum values of the normalized excess pore water pressure rate each load cycle are denoted as $\dot{u}_{\max}/p'_o$ and $\dot{u}_{\min}/p'_o$, respectively. Figure 3 presents $\dot{u}_{\max}/p'_o$ and $\dot{u}_{\min}/p'_o$ versus $T$ for different $\eta$ values at $f = 1$ Hz with CSR = 0.20. Herein, both $\dot{u}_{\max}/p'_o$ and $\dot{u}_{\min}/p'_o$ decrease rapidly and then gradually tend to be zero after about $T = 100$ s.

## 3.2 Influence of cyclic stress ratio

Figure 4 presents excess pore water pressure versus the number of cycles with different CSRs under $f = 1.0$ Hz and $\eta = 1.00$. Herein, with increasing of CSR, both $u_{\max}$ and $u_{\min}$ increase under the same number of cycles. For example, in Figure 4, at the end of 10,000 cycles, the $u_{\max}$ are 21.11, 39.10, 59.26, and 85.32 kPa, and $u_{\min}$ are 13.41, 20.31, 30.08, and 45.76 kPa at CSR = 0.10, 0.15, 0.20, and 0.30, respectively.
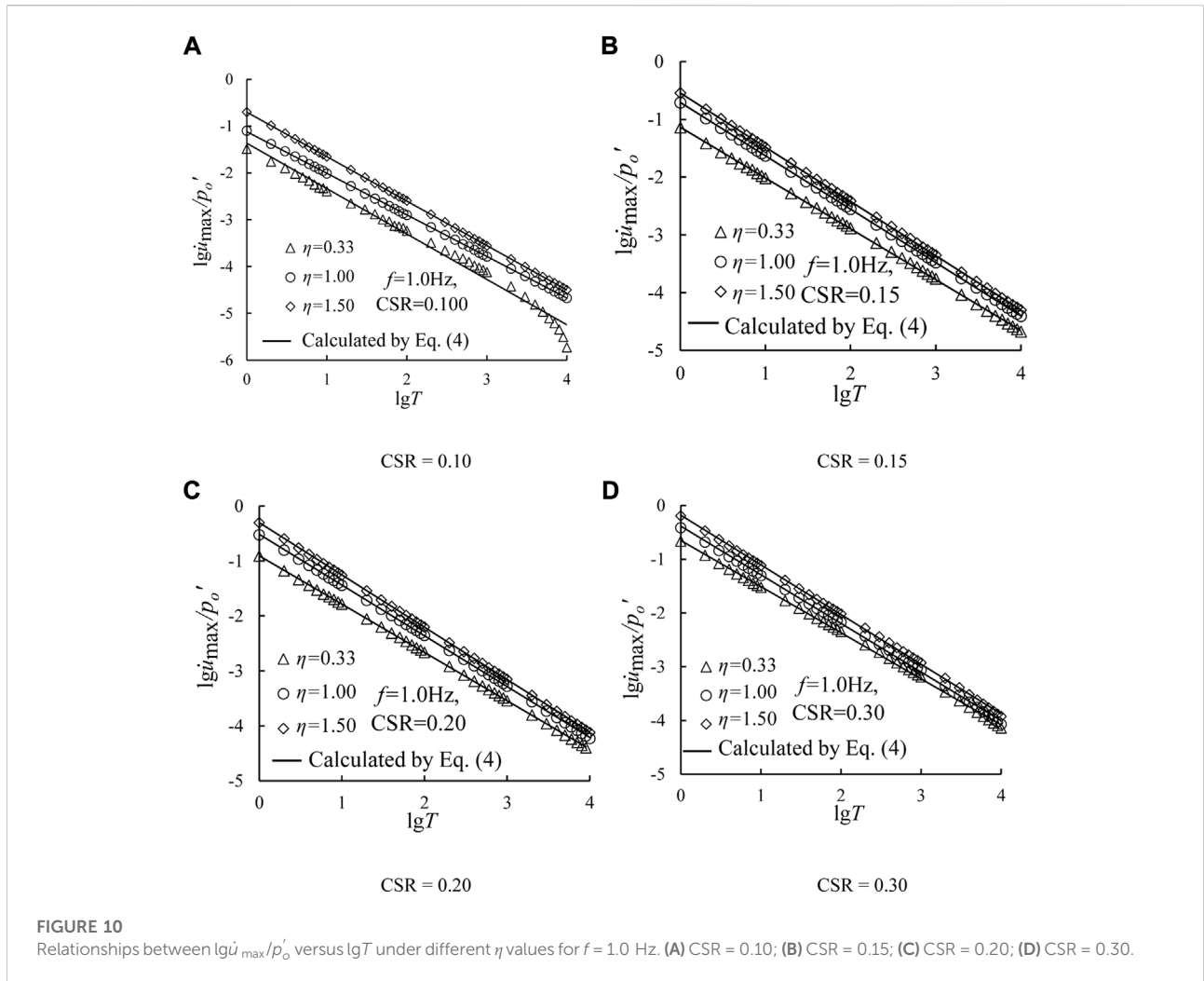
**FIGURE 10**
Relationships between $\lg \dot{u}_{max}/p'_o$ versus $\lg T$ under different $\eta$ values for $f = 1.0$ Hz. **(A)** CSR = 0.10; **(B)** CSR = 0.15; **(C)** CSR = 0.20; **(D)** CSR = 0.30.

**TABLE 4 Fitting parameters of Eqs 4, 5.**

| CSR | $\eta$ | $\lg\dot{u}_{max}/p'_o = A\lg T + \lg(\dot{u}_{max}/p'_o)_{T=1}$ | | | $\lg\dot{u}_{min}/p'_o = a\lg T + \lg(\dot{u}_{min}/p'_o)_{T=1}$ | | |
|---|---|---|---|---|---|---|---|
| | | $A$ | $\lg(\dot{u}_{max}/p'_o)_{T=1}$ | $R^2$ | $a$ | $\lg(\dot{u}_{min}/p'_o)_{T=1}$ | $R^2$ |
| 0.10 | 1/3 | −0.970 | −1.366 | 0.986 | −0.764 | −1.927 | 0.907 |
| | 1.0 | −0.888 | −1.120 | 1.000 | | | |
| | 1.5 | −0.950 | −0.703 | 1.000 | | | |
| 0.15 | 1/3 | −0.880 | −1.134 | 0.999 | −0.772 | −1.563 | 0.983 |
| | 1.0 | −0.925 | −0.705 | 1.000 | | | |
| | 1.5 | −0.939 | −0.542 | 1.000 | | | |
| 0.20 | 1/3 | −0.880 | −0.904 | 0.999 | −0.783 | −1.334 | 0.992 |
| | 1.0 | −0.924 | −0.513 | 0.999 | | | |
| | 1.5 | −0.952 | −0.302 | 1.000 | | | |
| 0.30 | 1/3 | −0.858 | −0.653 | 0.999 | −0.758 | −1.093 | 0.986 |
| | 1.0 | −0.905 | −0.385 | 0.999 | | | |
| | 1.5 | −0.924 | −0.182 | 0.999 | | | |

$\lg(\dot{u}_{max}/p'_o)_{T=1}$: normalized maximum excess pore water pressure rate at a unit time;
$\lg(\dot{u}_{min}/p'_o)_{T=1}$: normalized minimum excess pore water pressure rate at a unit time;
$A$, is expressed as the decay rate of normalized maximum excess pore water pressure rate with time in logarithmic coordinates;
$a$ is expressed as the decay rate of normalized minimum excess pore water pressure rate with time in logarithmic coordinates;
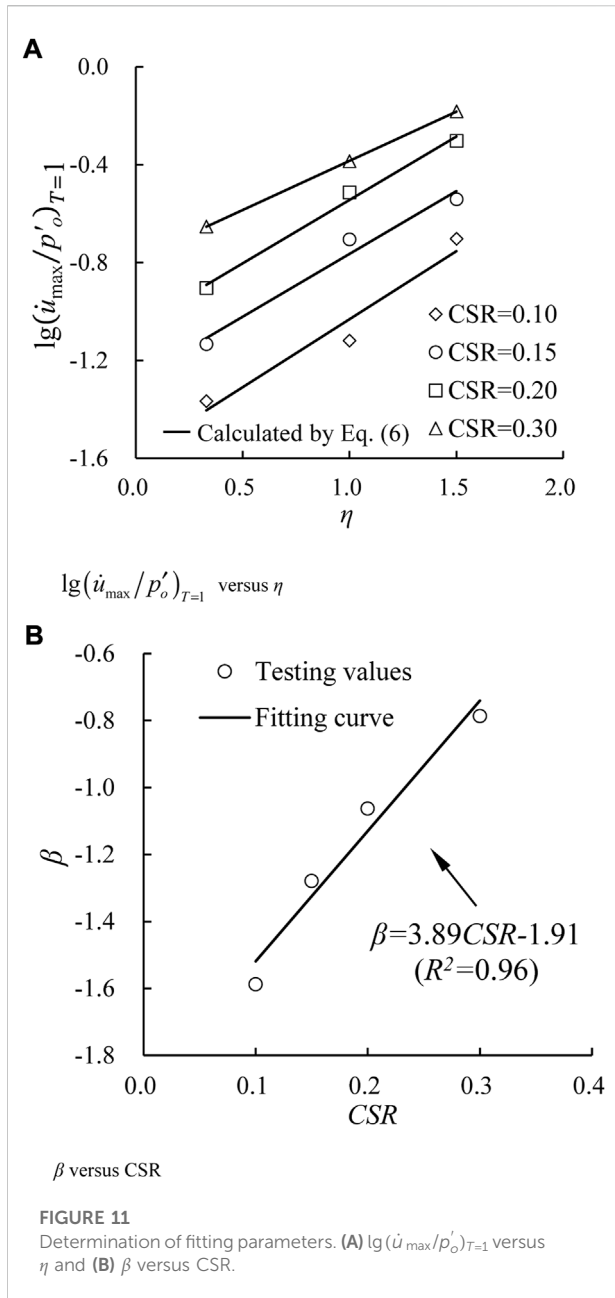$\eta$ is the slope of stress path.

**FIGURE 11**
Determination of fitting parameters. **(A)** $\lg(\dot{u}_{\max}/p_o')_{T=1}$ versus $\eta$ and **(B)** $\beta$ versus CSR.

TABLE 5 Fitting parameters of Eq. 6.

| CSR | $\alpha$ | $\beta$ | $R^2$ |
|-----|----------|---------|-------|
| 0.10 | 0.556 | −1.588 | 0.948 |
| 0.15 | 0.514 | −1.278 | 0.972 |
| 0.20 | 0.519 | −1.062 | 0.993 |
| 0.30 | 0.402 | −0.786 | 1.000 |

To quantify the influence of CSR on excess pore water pressure, both $u_{\max}$ and $u_{\min}$ at 10,000 cycles (denoted as $u_{\max,10000}$, and $u_{\min,10000}$, respectively) versus CSRs are plotted in Figure 5. As it is seen, both $u_{\max}$ and $u_{\min}$ are linearly increasing with increasing CSRs. Therefore, the relationships between $u_{\max,10000}$, $u_{\min,10000}$ and CSR can be expressed by two linearly increasing functions, as follows:

$$u_{\max,10000} = e + f \cdot CSR \tag{1}$$

$$u_{\min,10000} = m + n \cdot CSR \tag{2}$$

where $e$, $f$, $m$, and $n$ are fitting parameters. Table 3 summarizes the fitting parameters by using regression analysis and the respective curves are shown as the dotted lines in Figure 5. It is observed that the Eqs 1, 2 have a good prediction capability to $u_{\max,10000}$, and $u_{\min,10000}$ with high correlation coefficients for all the cases.

Again, taking the test results of $\eta = 1.0$ and $f = 1$ Hz as an example, the relationships between $\dot{u}_{\max}/p_o'$, $\dot{u}_{\min}/p_o'$ and $T$ for different CSRs are plotted in Figure 6.

Herein, both $\dot{u}_{\max}/p_o'$ and $\dot{u}_{\min}/p_o'$ decrease rapidly and tend to a steady-state (i.e., 0 value) after a certain number of cycles, implying that most of excess pore water pressure has been accumulated during the beginning few cycles, following that, the surplus pore water pressure rises at significantly slower rates as the test progresses.
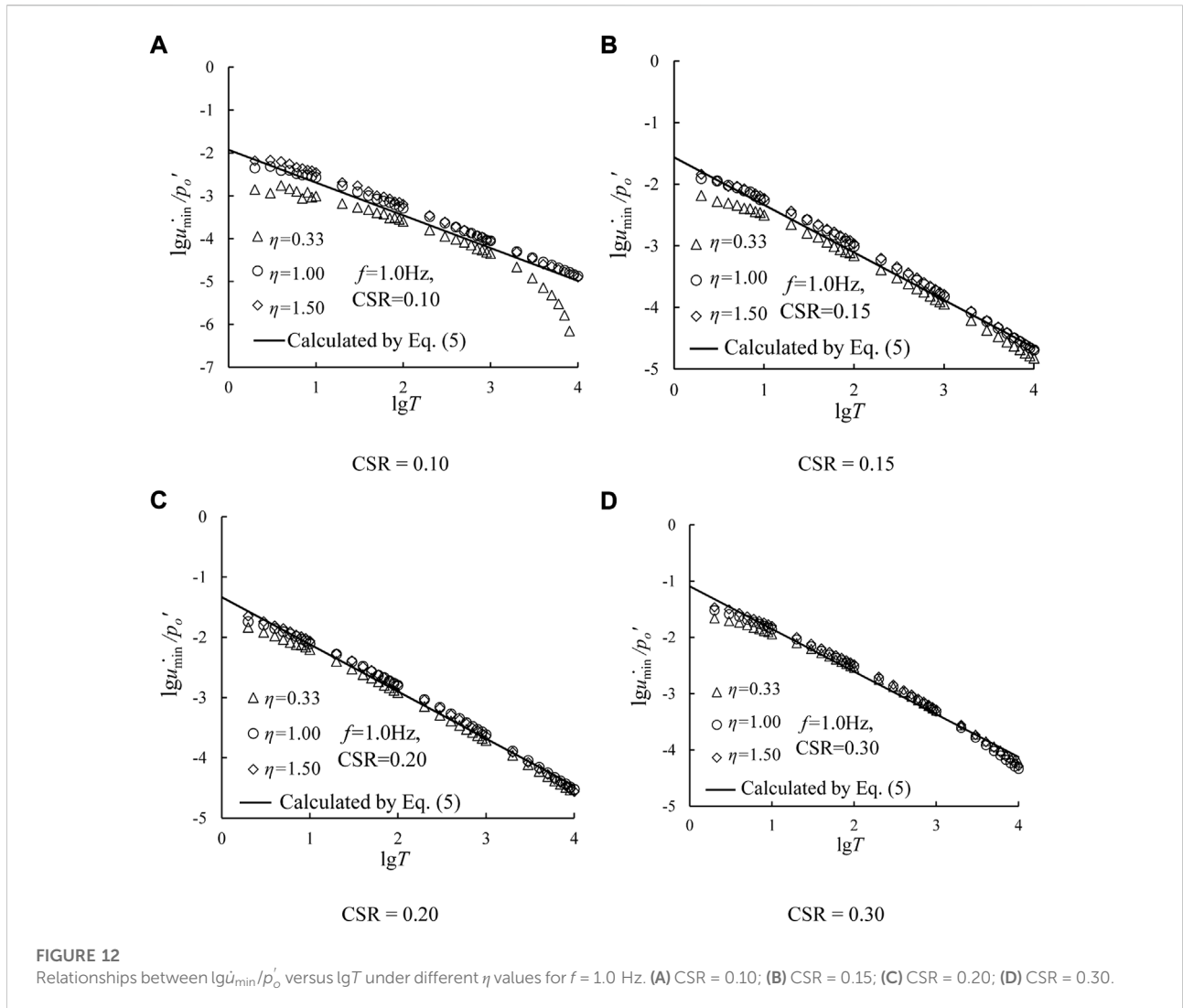
## 3.3 Influence of loading frequency

Figure 7 presents the relationship between excess pore water pressure and the number of cycles for different loading frequencies under CSR = 0.20 and $\eta = 1.5$. Herein, both $u_{\max}$ and $u_{\min}$ generally accumulate rapidly at the beginning and then achieve a stable state regardless of the various frequencies. Additionally, as seen in Figure 7, at the end of tests (i.e., $N=10,000$), when $f = 0.5$, 1.0, and 2.0 Hz, the $u_{\max}$ are 79.36, 75.98, and 69.86 kPa, while the $u_{\min}$ are 32.20, 27.70, and 28.91 kPa, respectively, indicating that the lower loading frequency can deliver the greater excess pore water pressure. The phenomenon is related to the permeability of soft clay. When a low frequency is applied to the specimen, the excess pore water pressure induced in every single cycle has much more time to develop, while the accumulation time of excess pore water pressure is much smaller under greater loading frequency.

Again, the relationships between $\dot{u}_{\max}/p_o'$, $\dot{u}_{\min}/p_o'$ and $T$ for different loading frequencies under the same test conditions (i.e., CSR = 0.20 and $\eta = 1.5$) are shown in Figure 8. Herein, the trends of all curves are similar and most of the test data are concentrated on the same curve, implying that the effects of loading frequency on the development of $\dot{u}_{\max}/p_o'$ and $\dot{u}_{\min}/p_o'$ against $T$ can be ignored.

## 3.4 Modified models for excess pore water pressure considering several factors

Based on many previous researches, some empirical formulas to predict excess pore water pressure were obtained. The previous

**FIGURE 12**
Relationships between $\lg\dot{u}_{min}/p_o'$ versus $\lg T$ under different $\eta$ values for $f$ = 1.0 Hz. **(A)** CSR = 0.10; **(B)** CSR = 0.15; **(C)** CSR = 0.20; **(D)** CSR = 0.30.

formulas were established based on the test results of the relationships between several factors and excess pore water pressure, while the researches on excess pore water pressure rate under cyclic loading were few. Besides that, the effect of cyclic confining pressure was hardly incorporated into the previous formulas. Following the research by Hyde and Ward (1985), the relationship between $\dot{u}/p_o'$ and $T$ in a log-log plot can be obtained as follows:

$$\lg\dot{u}\Big/p_o' = A\lg T + \lg\left(\frac{\dot{u}}{p_o'}\right)_{T=1}, \qquad (3)$$

where $(\dot{u}/p_o')_{T=1}$ = the normalized excess pore water pressure rate at a unit time; $A$ = the gradient of the $\lg\dot{u}/p_o'$ - $\lg T$ plot.

However, according to the above test results, several factors, such as CSR, cyclic confining pressure, and loading frequency have different influences on the $u_{max}$ and $u_{min}$. Thus, based on

the Eq. 3, the predicted formulas for $u_{max}$ and $u_{min}$ can be obtained as follows:

$$\lg\dot{u}_{max}\Big/p_o' = A\lg T + \lg\left(\dot{u}_{max}\Big/p_o'\right)_{T=1}, \qquad (4)$$

$$\lg\dot{u}_{min}\Big/p_o' = a\lg T + \lg\left(\dot{u}_{min}\Big/p_o'\right)_{T=1}, \qquad (5)$$

where $\lg(\dot{u}_{max}/p_o')_{T=1}$, $\lg(\dot{u}_{min}/p_o')_{T=1}$ = the normalized maximum and minimum excess pore water pressure rate at a unit time; $A$, and $a$ are expressed as the decay rate of normalized maximum and minimum excess pore water pressure rate with time in logarithmic coordinates.

However, Eqs 4, 5 cannot reflect explicitly the effects of cyclic confining pressure and CSR on excess pore water pressure rate. Therefore, it is necessary to modify the parameters of the Eqs 4, 5 (i.e., $A$, $a$, $\lg(\dot{u}_{max}/p_o')_{T=1}$, and $\lg(\dot{u}_{min}/p_o')_{T=1}$) considering the impacts of cyclic confining pressure, cyclic stress ratio, and loading frequency.

**FIGURE 13**
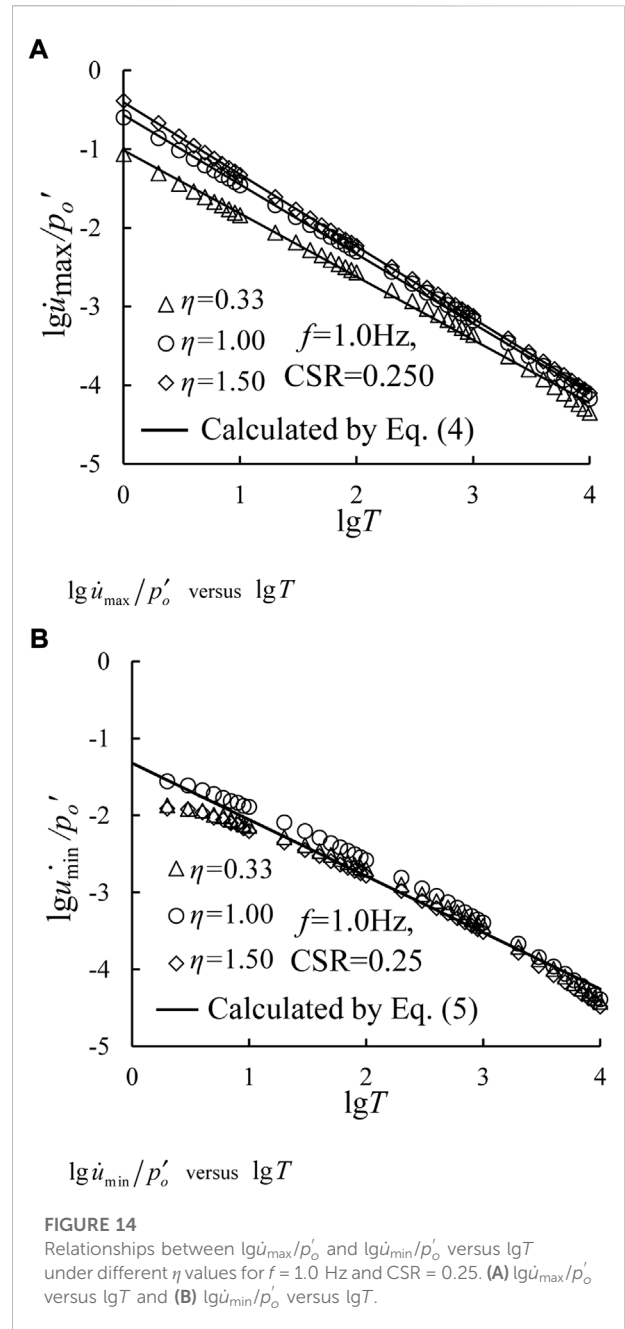Relationship between $\lg(\dot{u}_{\min}/p'_o)_{T=1}$ and CSRs.
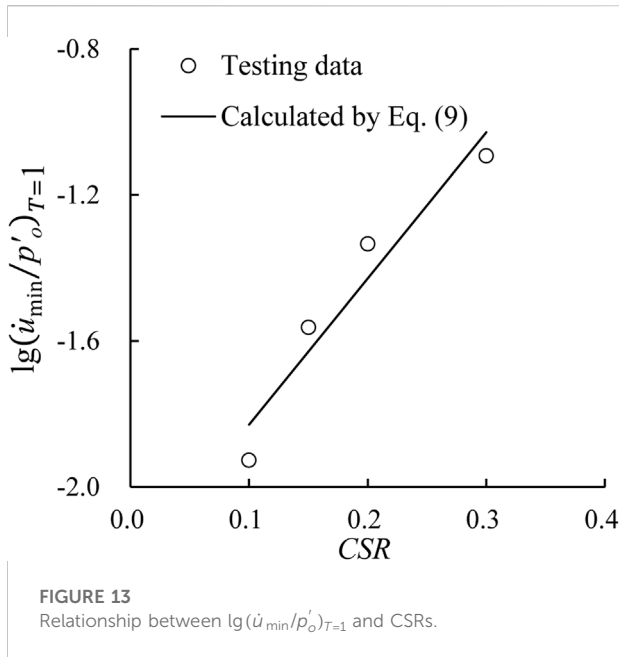
### 3.4.1 Influence of frequency on fitting parameters

Figure 9 shows $\lg\dot{u}_{\max}/p'_o$ and $\lg\dot{u}_{\min}/p'_o$ versus $\lg T$ for different loading frequencies based on the results of Figure 8. As seen, most of the test data are concentrated on the same curve, implying the fitting parameters are independent of loading frequency. The Eqs 4, 5 are taken to fit the test data in Figures 9A,B. Then, the fitting parameters of Eqs 4, 5 are obtained and the fitting curves are shown as red solid lines in Figure 9. It is seen that Eqs 4, 5 have a good prediction capability for maximum and minimum excess pore water pressure with high correlation coefficients. Additionally, the fitting parameters of $\lg(\dot{u}_{\max}/p'_o)_{T=1}$, $\lg(\dot{u}_{\min}/p'_o)_{T=1}$, $A$, and $a$ are −0.335, −1.195, −0.943, and −0.815 under different loading frequencies.

### 3.4.2 Influences of cyclic stress ratio and cyclic confining pressure on fitting parameters

Figure 10 plots the relationships between $\lg\dot{u}_{\max}/p'_o$ and $\lg T$ with varying $\eta$ values, in which Figures 10A–D are the results for CSR = 0.10, 0.15, 0.20, and 0.30, respectively. As seen, the $\lg\dot{u}_{\max}/p'_o$ - $\lg T$ lines with different $\eta$ values have identical inclinations. Table 4 summarizes the fitting parameters of Eq. 4 by regression analysis. As seen, although there are some variations in the fitting coefficient $A$ (Eq. 4) for different test conditions, these variations are not related to the CSR and $\eta$ values for the reason that the standard deviation of $A$ is so small (i.e., 0.0341). Therefore, the fitting parameter $A$ can be represented with the mean value of all $A$ values (i.e., $\bar{A}$ = −0.916). Recalling Table 4, the parameter $\lg(\dot{u}_{\max}/p'_o)_{T=1}$ is further studied with CSR and $\eta$ values. In Figure 11A, the parameter $\lg(\dot{u}_{\max}/p'_o)_{T=1}$ is plotted versus $\eta$



**FIGURE 14**
Relationships between $\lg\dot{u}_{\max}/p'_o$ and $\lg\dot{u}_{\min}/p'_o$ versus $\lg T$ under different $\eta$ values for $f$ = 1.0 Hz and CSR = 0.25. **(A)** $\lg\dot{u}_{\max}/p'_o$ versus $\lg T$ and **(B)** $\lg\dot{u}_{\min}/p'_o$ versus $\lg T$.

values. As presented, $\lg(\dot{u}_{\max}/p'_o)_{T=1}$ increases linearly with $\eta$ for the different CSRs and can be expressed as

$$\lg(\dot{u}_{\max}/p'_o)_{T=1} = \alpha \cdot \eta + \beta \left(\eta \geq \frac{1}{3}\right), \qquad (6)$$

where $\alpha$ and $\beta$ are fitting parameters. Table 5 summarizes the values of parameters $\alpha$ and $\beta$ under different CSR values. Likely, the standard deviation of $\alpha$ is 0.066, implying that the parameter $\alpha$ can be regarded as a constant with a mean value, i.e., $\alpha$=0.498. Additionally, Figure 11B presents the variations of $\beta$ with CSRs, which can be proposed with a linear function, as follows:

TABLE 6 Fitting parameters of Eqs 4, 5 based on the test results from Gu (2012).

| CSR | $\eta$ | $\lg \dot{u}_{\max}/p_o' = A\lg T + \lg(\dot{u}_{\max}/p_o')_{T=1}$ | | | $\lg \dot{u}_{\min}/p_o' = a\lg T + \lg(\dot{u}_{\min}/p_o')_{T=1}$ | | |
|---|---|---|---|---|---|---|---|
| | | $A$ | $\lg(\dot{u}_{\max}/p_o')_{T=1}$ | $R^2$ | $a$ | $\lg(\dot{u}_{\min}/p_o')_{T=1}$ | $R^2$ |
| 0.157 | 1/3 | −0.903 | −1.070 | 0.999 | −0.835 | −1.561 | 0.992 |
| | 1.0 | −0.934 | −0.644 | 0.999 | | | |
| | 1.5 | −0.956 | −0.422 | 1.000 | | | |
| 0.208 | 1/3 | −0.898 | −0.893 | 0.999 | −0.790 | −1.538 | 0.949 |
| | 1.0 | −0.932 | −0.498 | 1.000 | | | |
| | 1.5 | −0.951 | −0.295 | 1.000 | | | |
| 0.261 | 1/3 | −0.890 | −0.750 | 0.998 | −0.753 | −1.528 | 0.954 |
| | 1.0 | −0.907 | −0.474 | 0.999 | | | |
| | 1.5 | −0.943 | −0.200 | 1.000 | | | |

$\lg(\dot{u}_{\max}/p_o')_{T=1}$: normalized maximum excess pore water pressure rate at a unit time;
$\lg(\dot{u}_{\min}/p_o')_{T=1}$: normalized minimum excess pore water pressure rate at a unit time;
$A$, is expressed as the decay rate of normalized maximum excess pore water pressure rate with time in logarithmic coordinates;
$a$ is expressed as the decay rate of normalized minimum excess pore water pressure rate with time in logarithmic coordinates;
$\eta$ is the slope of stress path.

$$\beta = \lambda \cdot CSR + \kappa, \qquad (7)$$

where $\lambda$ and $\kappa$ are fitting parameters. The parameters in Eq. 7 are obtained as $\lambda = 3.89$, and $\kappa = -1.91$, respectively.

By incorporating Eqs 6, 7 into Eq. 4, the expression for $\dot{u}_{\max}$ can be proposed:

$$\lg \dot{u}_{\max}/p_o' = \bar{A}\lg T + \alpha\eta + \lambda CSR + \kappa. \qquad (8)$$

Figure 12 plots the relationships between $\lg \dot{u}_{\min}/p_o'$ and $\lg T$ with varying $\eta$ values, in which Figures 12A–D are the results for CSR = 0.10, 0.15, 0.20, and 0.30, respectively. At the same CSR value, most of the test data are concentrated on the same curves, implying that the effect of cyclic confining pressure on the $\lg \dot{u}_{\min}/p_o'$ - $\lg T$ curve can be ignored. Table 4 also summarizes the fitting parameters of Eq. 5. The fitting curves are also shown as the solid lines in Figure 12. The calculation results match well with the test data for high correlation coefficients. Recalling Table 4, the standard deviation of $a$ is 0.0106, meaning that the variations of parameter $a$ of Eq. 5 can be ignored. Therefore, the parameter $a$ can be represented as the mean value of parameter $a$, i.e., $\bar{a} = -0.769$. Besides that, recalling Figure 12 and Table 4, the parameter $\lg(\dot{u}_{\min}/p_o')_{T=1}$ remains unchanged for different $\eta$ values with the same CSR, implying that the influence of $\eta$ on the $\lg(\dot{u}_{\min}/p_o')_{T=1}$ can be ignored. Figure 13 depicts the variations of $\lg(\dot{u}_{\min}/p_o')_{T=1}$ with CSRs. Herein, the $\lg(\dot{u}_{\min}/p_o')_{T=1}$ linearly increase with CSR, and can be written as

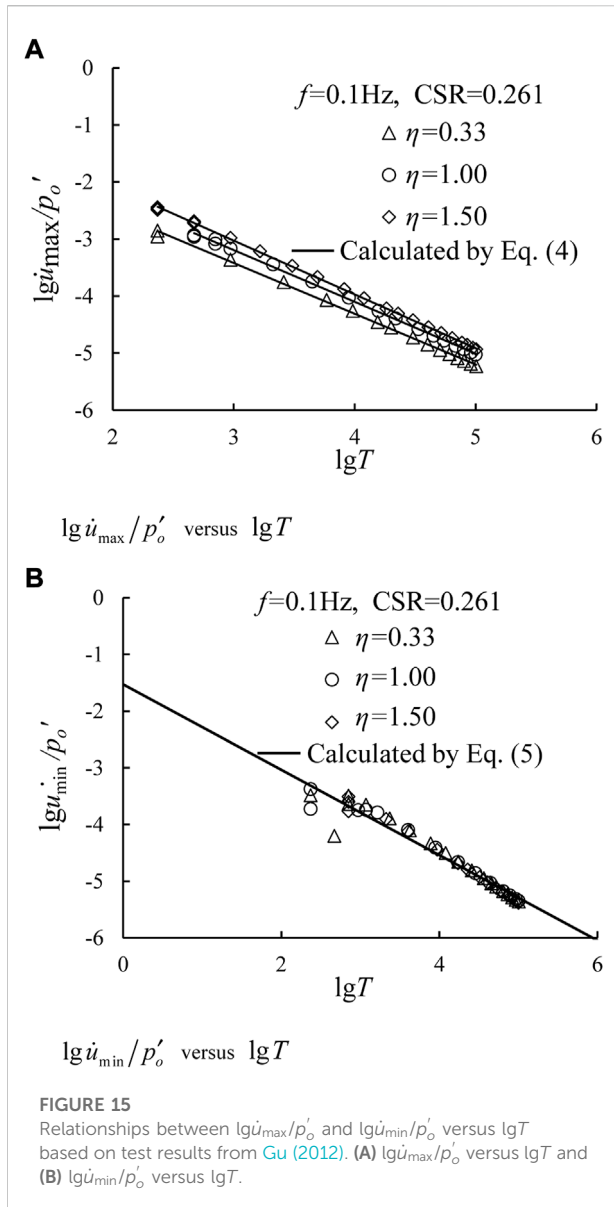$$\lg(\dot{u}_{\min}/p_o')_{T=1} = b \cdot CSR + d, \qquad (9)$$

where $b$ and $d$ are fitting parameters. Using the curve-fitting method, the parameter $c$ and $d$ are obtained as $b = 4.00$, and $d = -2.23$, respectively.

Then, setting the Eq. 9 into the Eq. 5 delivers:

$$\lg \dot{u}_{\min}/p_o' = \bar{a}\lg T + bCSR + d. \qquad (10)$$

### 3.4.3 Validation of modified models

To validate the accuracy of the proposed excess pore water pressure models (i.e., Eqs 4, 5, the test data for the test conditions, i.e., CSR = 0.25, $\eta$ = 0.33, 1.00, and 1.50 are employed. Figure 14 plots the variations in normalized excess pore water pressure rate with loading time. Herein, Figures 14A,B depict the development characteristics of maximum and minimum excess pore water pressure rate, respectively. Herein, the predicted values are also displayed as black solid lines by using Eqs 4, 5. As seen, the proposed empirical formula can well reproduce the test data, indicating that the proposed models have a better performance to depict the development of both maximum and minimum excess pore water pressure of soft clay under cyclic loading with cyclic confining pressure.

On the other hand, test results from Gu (2012) were taken as an example to validate the applicability of Eqs 4, 5. Among that, the employed CSRs were 0.157, 0.208, and 0.261. For a specific CSR, $\eta$ values were 1/3, 1.0, and 1.5, respectively. The loading frequency was 0.1 Hz. Taking Eqs 4, 5 to fit the test data, the fitting parameters of Eqs 4, 5 were obtained in Table 6. Figure 15 plots the relationships between normalized excess pore water pressure rate with loading time under CSR = 0.261 and $f$ = 0.1 Hz, in which Figures 15A,B depict the development characteristics of maximum and minimum excess pore water pressure rate, respectively. Herein, the predicted results agree well with the test data under different test conditions for high correlation coefficient. From Table 6, the standard deviations of parameters $A$ and $a$ are small, implying that the effects of CSR and cyclic confining pressure can be ignored. The mean values of parameter $A$ and $a$ can be employed in Eqs 4, 5. Additionally, the variations in $\lg(\dot{u}_{\max}/p_o')_{T=1}$ with $\eta$ for the different CSRs are similar to Figure 11, and the relationships between the

**FIGURE 15**
Relationships between $\lg\dot{u}_{max}/p_o'$ and $\lg\dot{u}_{min}/p_o'$ versus $\lg T$ based on test results from Gu (2012). **(A)** $\lg\dot{u}_{max}/p_o'$ versus $\lg T$ and **(B)** $\lg\dot{u}_{min}/p_o'$ versus $\lg T$.

(1) These factors, i.e., cyclic confining pressure, CSR, and loading frequency have different effects on the development of excess pore water pressure. With increasing $\eta$, $u_{max}$ increases, while $u_{min}$ remains unchanged. Additionally, the larger CSR can deliver greater both $u_{max}$ and $u_{min}$. Furthermore, the increase of the $u_{max}$ and $u_{min}$ with decreasing loading frequency is more significant.

(2) Both normalized maximum and minimum excess pore water pressure rates increase with increasing CSR and $\eta$ at the beginning of tests, and coincide after a certain time. However, the curves of the normalized excess pore water pressure rate - time coincide under different loading frequencies.

(3) The relationships between the normalized excess pore water pressure rate and the loading time are linear under CCP and VCP tests in logarithmic coordinates. Both maximum and minimum excess pore water pressure prediction models are proposed. Nevertheless, the effects of the above factors on fitting parameters $A$ and $a$ can be ignored. $\lg(\dot{u}_{max}/p_o')_{T=1}$ increases linearly with increasing CSR and cyclic confining pressure, while $\lg(\dot{u}_{min}/p_o')_{T=1}$ only increases linearly with increasing CSR.

Limited the performance of the test equipment (namely, the applied maximum frequency is 5.0 Hz), only the effect of lower frequency (less than 2.0 Hz) on the development of excess pore water pressure is discussed. Therefore, the applicability of the proposed models needs further study under higher loading frequency conditions and other soils.

## Data availability statement

The original contributions presented in the study are included in the article/Supplementary Material, further inquiries can be directed to the corresponding author.

## Author contributions

JeH and JnH were involved in the final development of the project and manuscript preparation. HW and JC wrote the manuscript draft. JC and SL analyzed the data. All authors: corrections, modifications, and final acceptation.

## Funding

$\lg(\dot{u}_{min}/p_o')_{T=1}$ and CSRs are similar to Figure 13. It means that the effects of cyclic confining pressure, CSR, and loading frequency on fitting parameters can also be depicted by Eqs 6 and 7 (8), (9), and (10). In conclusion, Eqs 4, 5 can be used to predict the $\dot{u}_{max}/p_o'$ and $\dot{u}_{min}/p_o'$ under CCP and VCP tests.

## 4 Conclusion

CCP and VCP tests were conducted on saturated soft clay to investigate the development of excess pore water pressure. The effects of CSR, cyclic confining pressure, and loading frequency were studied. The main conclusions can be drawn as follows:

## Conflict of interest

## Publisher's note

## References

ASTM (2017). *Standard practice for classification of soils for engineering purposes (Unified Soil Classification System)*. West Conshohocken, PA: ASTM.

Cai, Y. Q., Gu, C., Wang, J., Juang, C. H., Xu, C. J., and Hu, X. Q. (2013). One-way cyclic triaxial behavior of saturated clay: Comparison between constant and variable confining pressure. *J. Geotech. Geoenviron. Eng.* 139 (5), 797–809. doi:10.1061/(asce)gt.1943-5606.0000760

Cary, C. E., and Zapata, C. E. (2016). Pore water pressure response of soil subjected to dynamic loading under saturated and unsaturated conditions. *Int. J. Geomech.* 16 (6), D4016004. doi:10.1061/(asce)gm.1943-5622.0000642

Du, W. J., Sheng, Q., Fu, X. D., Chen, J., and Zhou, Y. Q. (2022). A TPDP-MPM-based approach to understanding the evolution mechanism of landslide-induced disaster chain. *J. Rock Mech. Geotechnical Eng.* 14 (4), 1200–1209. doi:10.1016/j.jrmge.2022.03.004

Fu, X. D., Ding, H. F., Sheng, Q., Zhang, Z. P., Yin, D. W., and Chen, F. (2022). Fractal analysis of particle distribution and scale effect in a soil-rock mixture. *Fractal Fract.* 6 (2), 120. doi:10.3390/fractalfract6020120

GB/T 50123-2019 (2019). *Standard for geotechnical testing method (GB/T 50123-2019)*. Beijing: China Planning Press.

Gu, C., Gu, Z. Q., Cai, Y. Q., Wang, J., and Ling, D. S. (2017). Dynamic modulus characteristics of saturated clays under variable confining pressure. *Can. Geotech. J.* 54 (5), 729–735. doi:10.1139/cgj-2016-0441

Gu, C. (2012). Study on the dynamic behavior of saturated clays based on the stress paths with variable confining pressure. China: College of Civil Engineering and Architecture. Ph.D. thesis.

Gu, C., Wang, J., Cai, Y. Q., Sun, L., Wang, P., and Dong, Q. Y. (2016). Deformation characteristics of overconsolidated clay sheared under constant and variable confining pressure. *Soils Found.* 56 (3), 427–439. doi:10.1016/j.sandf.2016.04.009

Gu, C., Wang, J., Cai, Y. Q., Yang, Z. X., and Gao, Y. F. (2012). Undrained cyclic triaxial behavior of saturated clays under variable confining pressure. *Soil Dyn. Earthq. Eng.* 40, 118–128. doi:10.1016/j.soildyn.2012.03.011

Guo, L., Chen, J. M., Wang, J., Cai, Y. Q., and Deng, P. (2016). Influences of stress magnitude and loading frequency on cyclic behavior of $K_0$-consolidated marine clay involving principal stress rotation. *Soil Dyn. Earthq. Eng.* 84, 94–107. doi:10.1016/j.soildyn.2016.01.024

Guo, L., Wang, J., Cai, Y. Q., Liu, H. L., Gao, Y. F., and Sun, H. L. (2013). Undrained deformation behavior of saturated soft clay under long-term cyclic loading. *Soil Dyn. Earthq. Eng.* 50, 28–37. doi:10.1016/j.soildyn.2013.01.029

Huang, F. M., Cao, Z. S., Guo, J. F., Jiang, S. H., and Guo, Z. Z. (2020a). Comparisons of heuristic, general statistical and machine learning models for landslide susceptibility prediction and mapping. *Catena* 191, 104580. doi:10.1016/j.catena.2020.104580

Huang, F. M., Zhang, J., Zhou, C. B., Wang, Y. H., Huang, J. S., and Zhu, L. (2020b). A deep learning algorithm using a fully connected sparse autoencoder neural network for landslide susceptibility prediction. *Landslides* 17 (1), 217–229. doi:10.1007/s10346-019-01274-9

Huang, J. H., Chen, J., Lu, Y., Yi, S., Cheng, H. Z., and Cui, L. (2020). Deformation behaviors and dynamic backbone curve model of saturated soft clay under bidirectional cyclic loading. *Int. J. Geomech.* 20 (4), 04020016. doi:10.1061/(asce)gm.1943-5622.0001628

Hyde, A. F. L., and Ward, S. J. (1985). A pore pressure and stability model for a silty clay under repeated loading. *Geotechnique* 35 (2), 113–125. doi:10.1680/geot.1985.35.2.113

Hyde, A. F. L., Yasuhara, K., and Hirao, K. (1993). Stability criteria for marine clay under one-way cyclic loading. *J. Geotech. Engrg.* 119 (11), 1771–1789. doi:10.1061/(asce)0733-9410(1993)119:11(1771)

Hyodo, M., Yasuhara, K., and Hirao, K. (1992). Prediction of clay behaviour in undrained and partially drained cyclic triaxial tests. *Soils Found.* 32 (4), 117–127. doi:10.3208/sandf1972.32.4_117

Jiang, S. H., Huang, J., Huang, F. M., Yang, J. H., Yao, C., and Zhou, C. B. (2018). Modelling of spatial variability of soil undrained shear strength by conditional random fields for slope reliability analysis. *Appl. Math. Model.* 63, 374–389. doi:10.1016/j.apm.2018.06.030

Lekarp, F., Isacsson, U., and Dawson, A. (2000). State of the art. I: Resilient response of unbound aggregates. *J. Transp. Eng.* 126 (1), 66–75. doi:10.1061/(asce)0733-947x(2000)126:1(66)

Matsui, T., Bahr, M. A., and Abe, N. (1992). Estimation of shear characteristics degradation and stress-strain relationship of saturated clays after cyclic loading. *Soils Found.* 32 (1), 161–172. doi:10.3208/sandf1972.32.161

Nie, Q., Bai, B., Hu, J., and Shang, W. (2007). The pore pressure model and undrained shear strength of soft clay under cyclic loading. *Rock Soil Mech.* 28, 724–729. doi:10.16285/j.rsm.2007.s1.155

Ohara, S., and Matsuda, H. (1988). Study on the settlement of saturated clay layer induced by cyclic shear. *Soils Found.* 28 (3), 103–113. doi:10.3208/sandf1972.28.3_103

Paul, M., Sahu, R. B., and Banerjee, G. (2014). Undrained pore pressure prediction in clayey soil under cyclic loading. *Int. J. Geomech.* 15 (5), 04014082. doi:10.1061/(asce)gm.1943-5622.0000431

Ren, X. W., Xu, Q., Xu, B. C., Teng, J. D., and Lv, S. H. (2018). Undrained pore pressure behavior of soft marine clay under long-term low cyclic loads. *Ocean. Eng.* 150, 60–68. doi:10.1016/j.oceaneng.2017.12.045

Rondon, H. A., Wichtmann, T., Triantafyllidis, T., and Lizcano, A. (2009). Comparison of cyclic triaxial behavior of unbound granular material under constant and variable confining pressure. *J. Transp. Eng.* 135 (7), 467–478. doi:10.1061/(asce)te.1943-5436.0000009

Sakai, A., Samang, L., and Miura, N. (2003). Partially-drained cyclic behavior and its application to the settlement of a low embankment road on silty-clay. *Soils Found.* 43 (1), 33–46. doi:10.3208/sandf.43.33

Sun, L., Cai, Y. Q., Gu, C., Wang, J., and Guo, L. (2015). Cyclic deformation behaviour of natural $K_0$ - consolidated soft clay under different stress paths. *J. Cent. South Univ.* 22, 4828–4836. doi:10.1007/s11771-015-3034-4

Tang, Y. Q., Cui, Z. D., Zhang, X., and Zhao, S. K. (2008). Dynamic response and pore pressure model of the saturated soft clay around the tunnel under vibration loading of Shanghai subway. *Eng. Geol.* 98 (3-4), 126–132. doi:10.1016/j.enggeo.2008.01.014

Wang, J., Guo, L., Cai, Y. Q., Bian, X. C., and Gu, C. (2013). Strain and pore pressure development on soft marine clay in triaxial tests with a large number of cycles. *Ocean. Eng.* 74, 125–132. doi:10.1016/j.oceaneng.2013.10.005

Wang, Y., Zhang, S. X., Yin, S., Liu, X. Y., and Zhang, X. W. (2020). Accumulated plastic strain behavior of granite residual soil under cycle loading. *Int. J. Geomech.* 20 (11), 04020205. doi:10.1061/(asce)gm.1943-5622.0001850

Wichtmann, K., Andersen, K. H., Sjursen, M. A., and Berre, T. (2013). Cyclic tests on high-quality undisturbed block samples of soft marine Norwegian clay. *Can. Geotech. J.* 50 (11), 400–412. doi:10.1139/cgj-2011-0390

Wichtmann, T., Niemunis, A., and Triantafyllidis, T. H. (2007). On the influence of the polarization and the shape of the strain loop on strain accumulation in sand under high-cyclic loading. *Soil Dyn. Earthq. Eng.* 27 (1), 14–28. doi:10.1016/j.soildyn.2006.05.002

Yang, Q., Tang, Y. Q., Yuan, B., and Zhou, J. (2018). Cyclic stress–strain behaviour of soft clay under traffic loading through hollow cylinder apparatus: Effect of loading frequency. *Road Mater. Pavement Des.* 20 (5), 1026–1058. doi:10.1080/14680629.2018.1428219

Zhou, Y. Q., Sheng, Q., Li, N. N., and Fu, X. D. (2022). The dynamic mechanical properties of a hard rock under true triaxial damage-controlled dynamic cyclic loading with different loading rates: A case study. *Rock Mech. Rock Eng.* 55 (4), 2471–2492. doi:10.1007/s00603-021-02756-w